Thermodynamic modeling and electronic properties of $CsPb_{1-x}Sn_xI_3$ as a polymorphic alloy

Luis Octavio de Araujo [a,*], Celso R.C. Rêgo [b], Wolfgang Wenzel [b], Carlos Maciel de Oliveira Bastos [c], Maurício J. Piotrowski [d], Alexandre C. Dias [e], Diego Guedes-Sobrinho [a,*]

[a] Department of Chemistry, Federal University of Paraná, Curitiba, PR 81531-980, Brazil
[b] Institute of Nanotechnology Hermann-von-Helmholtz-Platz, Karlsruhe Institute of Technology, Karlsruhe 76021, Germany
[c] São Carlos Institute of Physics, University of São Paulo, São Carlos, SP 13566-590, Brazil
[d] Department of Physics, Federal University of Pelotas, Pelotas, RS 96010-900, Brazil
[e] Physical Institute and International Center for Physics, University of Brasília, Brasília, DF 70919-970, Brazil

Keywords:
Metal halide perovskites (MHPs)
All-inorganic perovskite alloys
Generalized quasichemical approximation
Density functional theory
DFT-1/2

A B S T R A C T

We performed first-principles calculations combined with a statistical approach based on the generalized quasichemical approximation (GQCA) to study the polymorphic features of $CsPb_{1-x}Sn_xI_3$ alloy. Our analysis explored the impact of these polymorphic features on electronic properties, statistical attributes, and thermodynamic stability. Our findings indicate that $a^0a^0a^0$ ($Pm\bar{3}m$) polymorph makes only a minor contribution to alloy, while $a^-a^+a^-$ pattern has the highest probabilities at room temperature. Encompassing multiple polymorphic degrees within the same generalized ensemble, we found an increase in composition range where phase segregation becomes thermodynamically favored, albeit with a relatively low critical temperature (28.8 K). Despite this, our GQCA-PCE results obtained from the Spectroscopic Limited Maximum Efficiency (SLME) model reveal that the efficiency of alloy-based solar cells could be a little smaller than that of $CsSnI_3$ pure metal halide perovskite (MHP), in range 26.6 % → 30.7 % for $CsPbI_3$ → $CsSnI_3$ at 300 K, which would be compensated by the presence of Pb reducing the tendency of Sn-based MHPs to oxidize in air, favoring the fabrication of photovoltaic devices with enhanced long-term stability.

1. Introduction

Since the discovery of metal halide perovskites (MHPs) as promising materials for photovoltaic (PV) applications [1,2], hybrid compounds have been in the spotlight for their high power conversion efficiencies (PCE), which surpassed 26 % for $FAPbI_3$ single-junction devices [3], while $LBaMn_2O_{6-\gamma}$ (L = Nd, Sm, Eu, Gd, Tb) oxide perovskites have gained prominence for their magnetic and electrical properties [4]. The $FAPbI_3$ PCE is in line with those obtained for other photovoltaic technologies, such as crystalline silicon (26.8 %), GaAs (29.1 %), CIGS (23.35 %), and CdTe (21.0 %) [5,6], with the $FAPbI_3$ standing out for its simpler room temperature one-step possible synthesis procedure [7]. However, stability issues related to the organic cations in MHPs, due to their hygroscopic and volatile nature, have become challenging for developing long-lived solar cells (SCs) [8,9]. Thus, all-inorganic MHPs based on Cs have been proposed, with the black phase of $CsPbI_3$ being highlighted due to its smaller gap energy (1.73 eV) [10,11] in comparison with $CsPbBr_3$ (2.36 eV) [12] and $CsPbCl_3$ (3.00 eV) [12], since larger gap energies cause a reduction in the wavelengths range for the absorption of sunlight and, therefore, a reduced current that contributes to reduce the PCE [13]. However, for $CsPbI_3$, experimental reports pointed out it is stable only above 603 K [14], and the lack of organic cations with a random orientation in the cuboctahedral voids hinders entropic contributions that could stabilize it at room temperature [15]. Thus, its perovskite → non-perovskite phase transition is thermodynamically favored, leading to the degradation of the material's photovoltaic performance, which is even speeded up under air or light exposure [16,17].

Another issue regarding the application of $CsPbI_3$ in solar cells is the presence of toxic Pb, which could hinder their commercialization due to its restricted use in many countries [18]. Thus, to reduce Pb content in MHP compositions while stabilizing its photoactive phase, alloying $CsPbI_3$ with $CsSnI_3$ to form $CsPb_{1-x}Sn_xI_3$ would be a good strategy [19], since Pb and Sn have similar electronic structures and ionic radii (Pb^{2+}:

* Corresponding authors.
E-mail addresses: araujo.phys.chem@gmail.com (L.O. Araujo), guedessobrinho@ufpr.br (D. Guedes-Sobrinho).

1.03 Å, Sn^{2+}: 0.97 Å) [18,20,21]. In addition, the alloying strategy arises as a chemical alternative to the physical one based on crystal size modification, given that attempts to stabilize the cubic phase of $CsPbI_3$ using nanocrystals (NCs) tend to inhibit the charge transport in the resulting material [10,22,23].

Although the $CsPb_{1-x}Sn_xI_3$ alloy appears to be a promising candidate for PV devices, it has been considerably less explored experimentally for this application compared to its $(MA,FA)Pb_{1-x}Sn_xI_3$ hybrid counterparts [24]. Despite this, $CsPb_{1-x}Sn_xI_3$ has been demonstrated to be a good candidate for radiation detection, with $x = 0.50$ being capable of absorbing even the near-infrared (NIR-I) short wavelengths ($\approx$ 900 nm) [25], which makes it emerge as a promising material for tandem PV configurations as well [26,27].

Due to the scarcity of in-depth experimental studies on the properties of Pb/Sn-based all-inorganic alloys, first-principles calculations could be of great value in directing the synthesis of optimized materials for the manufacture of SCs. However, the construction of appropriate protocols considering the statistical nature of these materials, added to significant relativistic effects in their electronic structure – such as spin-orbit coupling (SOC) and quasiparticle (QP) approaches – is challenging [28,29], which becomes even more dramatic due to the complex structural polymorphism that MHPs manifest [30–33].

Recently, inorganic MHPs as polymorphous networks have arisen to the detriment of *Pm3̄m* structure, which manifests only as a macroscopic average over low-symmetry structural motifs due to the X-ray long coherence lenght [30,34]. These include B metal off-center displacements within the BX_6 octahedrons [35], second-order Jahn-Teller-like distortions [36], octahedrons rotations [37], and positional disorder of A within the cuboctahedral voids [15,32], contributing to the material's stabilization and being essential to good accordance between calculated and experimental MHPs properties [33]. However, in the case of alloys, the polymorphous nature of MHPs can be even more complex since the predominant structural motif can change with the system's composition and temperature, making it necessary to include this information in the proper statistical protocols.

The generalized quasichemical approximation (GQCA) [38] is a statistical protocol based on the cluster expansion (CE) formalism [39], making it possible to calculate several thermodynamic and structural properties as an average over the corresponding alloy's ensemble. Since MHPs have several sites to Pb ↔ Sn substitution, modeling these systems only based on supercells (SCs) without statistical considerations [40] is limited. Thus, even the statistical protocols already established in the literature may be limited since they usually consider a single type of structural motif for the entire alloy [41–44] and cannot wholly reflect the properties that would be experimentally verified.

In this work, we studied the thermodynamic, electronic properties, and statistical attributes of $CsPb_{1-x}Sn_xI_3$ alloy, investigating how its structural polymorphism modifies its properties under temperature effects. Through an utterly ab initio protocol based on the concept of all-polymorphic degrees (APD) generalized ensemble, we considered several polymorphic degrees of freedom within the same statistical framework. Our approach revealed the limitations of other protocols that consider only one polymorph in the calculation of the respective *T*-*x* phase diagram, allowing a theoretical modeling closer to experimental conditions than those based solely on DFT without explicit consideration of temperature effects [40,45]. By using such statistics and including QP through the affordable DFT-1/2 correction with SOC, we showed how the alloy's gap energy and PCE vary as a function of its composition *in operando* conditions, providing valuable insights for the rational design of all-inorganic SCs.

2. Methodology

2.1. Cluster Expansion and the Generalized Quasichemical Approximation (GQCA)

The properties of the $CsPb_{1-x}Sn_xI_3$ alloy were calculated through the GQCA, wherein its polymorphs were expanded into an ensemble of clusters that are statistically and energetically independent. The latter was constructed by considering $2 \times 2 \times 2$ SC expansions of a cubic unit cell (UC), with the Pb and Sn cations configured in 8 octahedral sites – as presented in Fig. 1 (a). By applying the symmetry operations associated with the *Pm3̄m* space group, the $2^8 = 256$ configurations were grouped into $J = 22$ classes – as schematized in Fig. 1 (b). The number of equivalent structures within each class is known as the degeneracy factor (g_j), satisfying the constraint $\sum_{j=1}^{J} g_j = 256$. Their values are listed in Table S1 of the Supporting Information.

By considering the $CsBI_3$ (B = Sn, Pb) MHPs as polymorphous networks, distortions from the ideal *Pm3̄m* structure were allowed to occur in the $CsPb_{1-x}Sn_xI_3$ alloy. This primarily included B metal off-center displacements within octahedra [35], positional rearrangements of Cs ions within the cuboctahedral cavities [36], and octahedrons rotations [37], the latter being denoted through the Glazer's notation [46]. In this notation, strings are associated with the magnitude (*a*, *b* or *c*), and superscripts with the relative orientation (e.g., a^0 for no rotation, a^+ in-phase, and a^- out-of-phase) of the rotations along each direction parallel to the crystal axes of our cubic SCs, as schematized in Fig. 1 (c). If the magnitude of rotation around two different axes is equivalent, the first string appearing in the notation is repeated, as detailed in Section II of the Supporting Information (Figure S1). Here, we use this notation to distinguish between the several polymorphs contributing for $CsPb_{1-x}Sn_xI_3$ ionic network, as described below.

To assess how the Glazer's patterns impact the structural and electronic properties of the $CsPb_{1-x}Sn_xI_3$ alloy, we initially selected five Glazer's patterns to configure the clusters expanding the alloy: $a^0a^0a^0$ (monomorphic *Pm3̄m* structure), $a^0b^+b^+$, $a^0b^-b^+$, $a^+a^-a^+$, $a^-a^-a^+$. This selection was based on our previous studies regarding the MHPs as polymorphous networks [31–33]. In addition, to consider the possibility of all these polymorphs in the alloy simultaneously, we constructed a generalized ensemble containing clusters from all structures (110 in total), termed as all polymorphic degrees (APD). Thus, APD ensemble is constructed by considering $a^0a^0a^0 + a^0b^+b^+ + a^0b^-b^+ + a^+a^-a^+ + a^-a^+a^-$. This generalized ensemble approach has been previously used to describe heterostructural alloys [47], and here it is modified to expand $CsPb_{1-x}Sn_xI_3$ in the cubic structure by considering several possibilities of structural motifs that can be present in its polymorphous networks [30,32]. A schematic representation of each Glazer's configuration mentioned above and APD can be verified in Section II of the Supporting Information (Figure S2).

When the temperature and pressure are fixed, and the latter is about 1 atm, the difference between the Gibbs and Helmholtz free energies is small (i.e. $G \approx F$) [47]. Thus, the thermodynamic behavior of the MHPs alloys can be described by using their mixing Helmholtz free energies, which is defined by

$$\Delta F(x,T) = \Delta U(x,T) \quad T\Delta S(x,T) \tag{1}$$

with $\Delta U(x, T)$ being the mixing internal energy and $\Delta S(x, T)$ the mixing entropy. The former is calculated as

$$\Delta U(x,T) = \sum_{j=1}^{J} x_j(x,T)\Delta\varepsilon_j \tag{2}$$

with $\Delta\varepsilon_j$ being named the excess energy of the *j*-th class, calculated through the expression

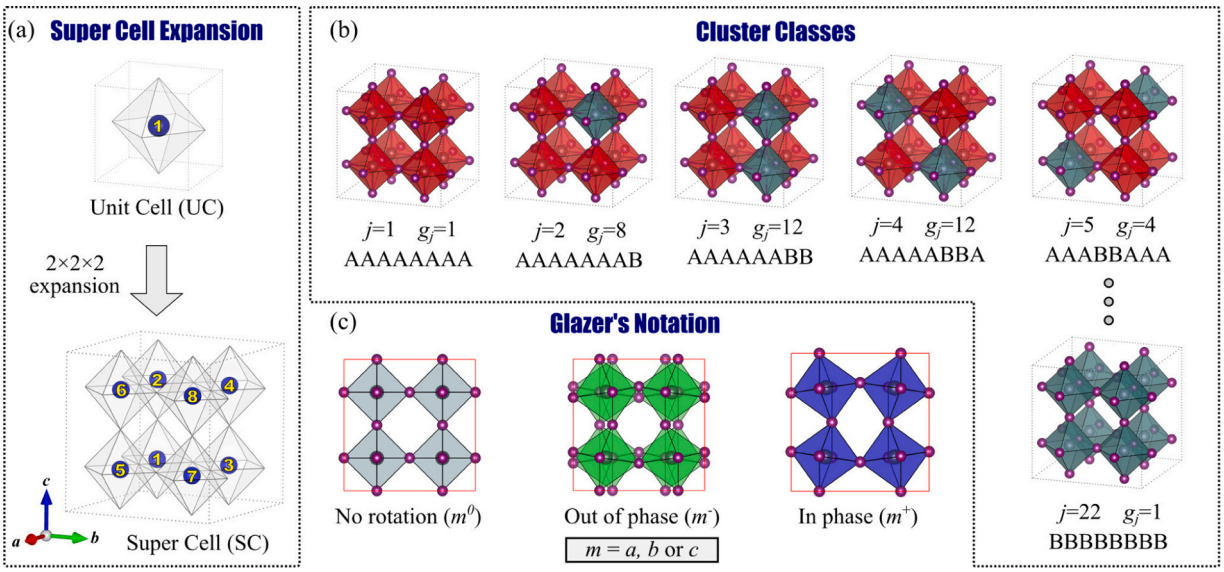

Fig. 1. Representation of (a) SC expansion of a cubic UC to form the cluster configurations expanding the $CsPb_{1-x}Sn_xI_3$ alloy and (b) the classes in which the clusters are grouped following the symmetry operations of the $Pm\bar{3}m$ space group of a cubic MHP structure. Octahedrons in red contain Pb at the center site, while those in green contain Sn. In the classes, the Pb is represented as A and Sn as B, following the sequence 12345678 of the site occupancies. (c) Schematic representation of the Glazer's notation, in which superscripts **0**, **-** and + indicate, respectively, no rotation (gray), out of phase (green), and in phase (blue) rotation around the ***m*** (***a***, ***b*** or ***c***) axis pointing out of the page's plane.

$$\Delta\varepsilon_j = E_j \quad \frac{n}{n} \quad \frac{n_j}{n} E_{CsPbI_3} \quad \frac{n_j}{n} E_{CsSnI_3} \tag{3}$$

In this, E_j, E_{CsPbI_3}, and E_{CsSnI_3} are the total energies of the j-th cluster, $CsPbI_3$ and $CsSnI_3$, respectively, obtained via DFT calculations, according to the procedure explained in subsection 2.3. In APD, we used the energy of the most stable polymorph for each pure MHP as a reference when constructing the graphs to make the effects of temperature on them clearer. n and n_j refer to the total number of octahedral sites (8 sites – Fig. 1 (a)) and the number of Sn cations in the cluster j. In Equation (2), x_j accounts for the cluster class probability, which is calculated as [43]

$$x_j(x,T) = \frac{g_j \eta^{n_j} e^{-\beta\Delta\varepsilon_j}}{\sum_{i=1}^{J} g_i \eta^{n_i} e^{-\beta\Delta\varepsilon_i}} \tag{4}$$

being $\beta = 1/k_B T$, k_B is the Boltzmann constant, T is the temperature, g_j is the degeneracy factor of j-th class and η is a parameter related to the constraint $\sum_j x_j(x,T) n_j = nx$. For APD, we also computed the polymorph probabilities as $x_k = \sum_{\forall j \in k} x_j$ – considering $k = a^0a^0a^0$, $a^0b^+b^+$, $a^0b\ b^+$, $a^+a\ a^+$ or $a\ a^+a$ – by summing over all clusters related to the corresponding k-th polymorph. Following this, the mixing entropy is defined as

$$\Delta S = \quad Nk_B[x\ln x + (1 \quad x)\ln(1 \quad x)] \quad Mk_B D_{KL}(x_j \| x_j^0) \tag{5}$$

in which N is the total number of cuboctahedral sites in the solid solution, and M is the total number of clusters in the alloy. $D_{KL}(x_j \| x_j^0)$ is the Kullback-Leibler (KL) divergence between the distributions $\{x_j\}$ and $\{x_j^0\}$, which is defined by [48]

$$D_{KL}(x_j \| x_j^0) = \sum_{j=1}^{J} x_j \ln\left(\frac{x_j}{x_j^0}\right) \tag{6}$$

with $x_j^0 = g_j x^{n_j}(1 \quad x)^{n \quad n_j}$ being the probability distribution for the j-th cluster in a regular solid solution, with the proper normalization to account for the number of polymorphs considered in the respective thermodynamic ensemble [38,41]. Previous works suggests that this expression is sufficient for calculating the thermodynamic properties of MHP alloys in good accordance with experiments [28,29,42,44], while for other systems, vibrational contributions could affect their stability and, if this happens, they should also be included in the entropic contributions. Based on the expression of ΔF, T-x phase diagrams were constructed by calculating the spinodal and binodal lines, as described below.

Through the Connolly-Williams method [41,49], electronic and structural properties (P) of the alloy were calculated as a weighted average over the respective properties from the clusters (P_j)

$$P(x,T) = \sum_{j=1}^{J} x_j(x,T) P_j \tag{7}$$

with $P(x, T)$ standing for lattice parameters (a, b and c), Pb–I distances, Pb–I–Pb angles, gap energies (E_g), among others. Furthermore, we also computed the statistical errors associated with fluctuations around the average values using the expression

$$\sigma_P(x,T) = \pm\left\{ \sum_{j=1}^{J} x_j(x,T) P_j^2 \quad P(x,T)^2 \right\}^{1/2} \tag{8}$$

2.2. The T-x phase diagram

The isobaric T-x phase diagrams reveal, for a range of temperatures, the compositions at which a mixture of $CsSnI_3$ and $CsPbI_3$ MHPs is expected to undergo phase segregation, metastability, or a complete solubilization, revealing the critical temperature (T_c) above which it will be stable as a random alloy for any value of x [50]. Within the region delineated by the binodal curve, calculated through the condition

$$\frac{\partial F}{\partial x}(x_a,T) = \frac{\partial F}{\partial x}(x_b,T) \tag{9}$$

phase segregation is thermodynamically favored, and the corresponding compositions of these segregated phases are given by x_a and x_b, respectively. However, even in this region, the alloy can show metastability against small local fluctuations in composition, as expressed by the spinodal curve [51]. The spinodal is calculated from the condition

$$\frac{\partial^2 F}{\partial x^2}(x_a',T) = \frac{\partial^2 F}{\partial x^2}(x_b',T) = 0 \tag{10}$$

indicating the metastability limit of the alloy at compositions $x = x_a^{'}$ and $x = x_b^{'}$. Thus, a complete miscibility gap is expected in the compositions range $x_a^{'} < x < x_b^{'}$, where mixing between $CsSnI_3$ and $CsPbI_3$ – at temperature T – is completely unfavorable.

2.3. DFT calculations

The total energy calculations and structural optimization relied on the density functional theory (DFT) [52,53], using the Perdew-Burke-Ernzerhof (PBE) [54] semilocal approximation for the exchange-correlation (XC) functional [55,56]. To solve the Kohn-Sham (KS) equations, we employed the projector augmented-wave method (PAW) [57], as implemented in the Vienna *Ab initio* Simulation Package (VASP). The valence states were treated within a scalar-relativistic (SR) approximation, which included SOC, while fully relativistic calculations accounted for the core states. The plane waves used within the PAW method were expanded up to a cutoff energy of 430 eV, and the following configurations were explicitly considered for the valence electrons: Cs ($5s^2$, $5p^6$, $6s^1$), Pb ($5s^2$, $5d^{10}$, $6s^2$, $6p^2$), Sn ($4d^{10}$, $5s^2$, $5p^2$) and I ($5s^2$, $5p^5$). The Brillouin zone (BZ) of our $2 \times 2 \times 2$ SC expansions was sampled by a $4 \times 4 \times 4$Γ-centered grid of **k** points. For the clusters with $a^0a^0a^0$ configuration, the lattice constants, stress tensors, and ions positions were fully optimized. For the other polymorphs, the lattice parameters were kept fixed at the $a^0a^0a^0$ optimum values, and only their respective ion positions were reoptimized. The total energy convergence criterion was set as 1.0×10^{-5} eV and the Hellmann-Feynman forces were relaxed until their values were less than 0.010 eV $Å^{-1}$ on every atom.

2.4. Gap energies from DFT-1/2 quasiparticle correction

The gap energies (E_g) were computed by employing the approximated QP correction named DFT-1/2 [58,59]. It is inspired by Slater's half-occupation technique [58,60] and is founded on Janak's theorem [61], which demonstrates that the orbital's energy eigenvalue with half-occupation equals the electron's ionization potential. The latter is calculated through a modified KS potential ($V_{mod,KS}(\mathbf{r})$), obtained by subtracting the self-energy potential ($V_S(\mathbf{r})$) from the standard KS potential ($V_{KS}(\mathbf{r})$), i.e. $V_{mod,KS}(\mathbf{r}) = V_{KS}(\mathbf{r}) \quad V_S(\mathbf{r})$. In such expression, $V_S(\mathbf{r})$ is acquired from the KS potentials associated with neutral ($V_0(\mathbf{r})$) and half-ionized atoms ($V_{-1/2}(\mathbf{r})$), with ionization performed from the 5*p* orbital of I [31,32]. Thus, $V_S(\mathbf{r}) = \Theta(\mathbf{r}, CUT)[V_0(\mathbf{r}) \quad V_{-1/2}(\mathbf{r})]$, where $\Theta(\mathbf{r}, CUT)$ is a step function introduced to prevent the potential interpenetration between neighbor atoms, whose optimal value of *CUT* parameter is determined through the maximization of the E_g values without empirical inferences [33]. Details about this variational procedure for $CsPbI_3$ and $CsSnI_3$ MHPs can be accessed in Section III of the Supporting Information (Figure S3). From this analysis, we determined that the *CUT* values for these compounds were 3.82 a_0 and 3.61 a_0, respectively, from which the *CUT* parameter for $CsPb_{1-x}Sn_xI_3$ is 3.72 a_0 [29].

2.5. PCE from the spectroscopy limited maximum efficiency (SLME) model

We used the spectroscopy limited maximum efficiency (SLME) model [62] to compute the power conversion efficiency (PCE) of $CsPb_{1-x}Sn_xI_3$ as a function of its composition, considering the MHP thickness $l = 1$ μm and $T = 300$ K. This model represents an advancement over the Shockley-Queisser (SQ) one [63], as it incorporates the film thickness (l) and the specific material's absorption coefficient ($\alpha(\omega)$). Detailed information about the model can be found in Section IV of Supporting Information.

To calculate the absorption coefficient ($\alpha_j(\omega)$) of each *j* expanding the polymorphs representing the $CsPb_{1-x}Sn_xI_3$ alloy, we also employed the DFT-1/2 QP correction with SOC, i.e. DFT-1/2+SOC. The expression [64,65]

$$\alpha_j(\omega) = \frac{\sqrt{2}\omega}{c}\left[\sqrt{\epsilon_{\mathrm{Re},j}^2(\omega) + \epsilon_{\mathrm{Im},j}^2(\omega)} \quad \epsilon_{\mathrm{Re},j}(\omega)\right]^{1/2}$$

was used, with $\hbar\omega$ being the photon energy, c denotes the speed of light in vacuum, $\epsilon_{\mathrm{Re},j}(\omega)$ is the real part, and $\epsilon_{\mathrm{Im},j}(\omega)$ the imaginary part of the dielectric function. $\epsilon_{\mathrm{Im},j}(\omega)$ was calculated using the random phase approximation (RPA) [66], while $\epsilon_{\mathrm{Re},j}(\omega)$ was obtained via the Kramers-Kronig transformation [67]. Following this, the absorption coefficient for alloy was obtained as a GQCA average over its respective ensemble, i.e. $\alpha(\omega; x, T) = \sum_{\forall j} x_j(x, T)\alpha_j(\omega)$ [29], using the cluster's total absorption coefficient by taking the *x*, *y* and *z* components of the dielectric tensor [68].

3. Results and discussion

3.1. Structural Properties

To understand the impact of mixing Pb and Sn cations on the structural behavior of $CsPb_{1-x}Sn_xI_3$, we start our discussion by analyzing its lattice parameter as a function of composition at room temperature. The averaged values calculated at $T = 300$ K for the $a^0a^0a^0$ polymorph are presented in Fig. 2 as a continuous curve, while those calculated for the clusters (*j*'s) representing the alloy are shown as scatter plots. Their numerical values can be accessed in Supporting Information (Table S2), whereas the averages calculated from the statistical distributions (x_j) associated with the other Glazer's configurations are available in Figure S4.

The calculated lattice parameters for the pristine $CsPbI_3$ (6.39 Å) and $CsSnI_3$ (6.28 Å) are in excellent agreement with the experimental reports (6.29 Å and 6.22 Å, respectively) [69–72] showing percent deviations smaller than 2 % for both compounds. In addition, the lattice constants approximately follow the Vegard's law [73], in which *a* value would decrease linearly with the tin content, correlating with the atomic radius of Sn (0.97 Å), which is approximately 5.8 % smaller than that of Pb (1.03 Å) [20,21].

The local structure of $CsPb_xSn_{1-x}I_3$ polymorphs was characterized by the B - I distances and B–I–B angles calculated for the alloy in all Glazer's configurations, whose results are shown in Fig. 3. By comparing the data from panels (b) and (c), we observed greater intervals covered by the highest and lowest B - I distances for $a^0b^+b^+$ configuration at both 0 K and 300 K, pointing to a suppressive effect that out-of-phase rotations in $a^0b^+b^+$ have on the B metal off-center displacements for the analyzed solid solution. This effect is further confirmed by the observations in

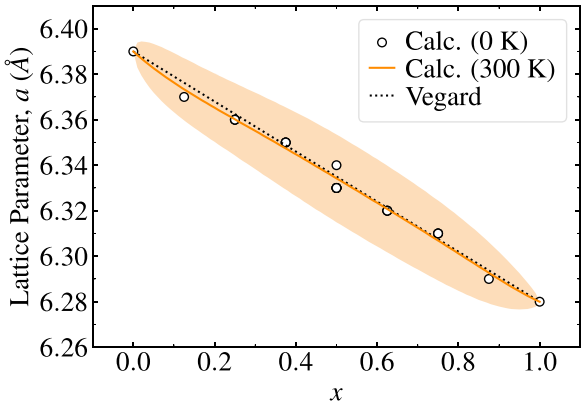

Fig. 2. Lattice parameter (a) calculated for the clusters (scatter) expanding the $CsPb_{1-x}Sn_xI_3$ alloys and its average value (solid orange line, 300 K) within the GQCA for $\boldsymbol{a^0a^0a^0}$ polymorph. The standard deviation of averaged values is indicated as a shaded orange region.

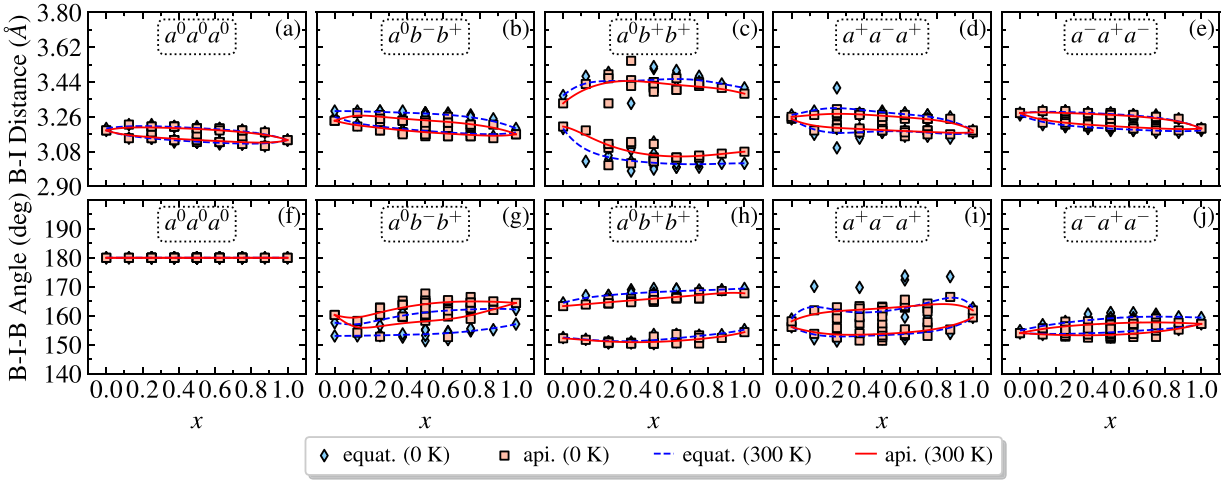

Fig. 3. Structural parameters calculated for clusters (scatter) and their average at 300 K calculated as a function of composition (x) for (a,f) $\boldsymbol{a^0a^0a^0}$, (b,g) $\boldsymbol{a^0b^-b^+}$, (c, h) $\boldsymbol{a^0b^+b^+}$, (d,i) $\boldsymbol{a^+a^-a^+}$, and (e,j) $\boldsymbol{a^-a^+a^-}$ polymorph of the $CsPb_{1-x}Sn_xI_3$ alloy.

panels (d) and (e), which suggest that structural motif tends to be similar to those of $a^0a^0a^0$ polymorph in panel (a), where it occurs mainly due to the mismatch between the Pb and Sn atomic radii occupying different B sites at the BI_3 sublattice. However, since such rotations improve the coordination environment of Cs by I, the smallest B - I distance increases even for the $CsPbI_3$ ($CsSnI_3$) pristine compound following 3.19 Å → 3.27 Å (3.14 Å → 3.19 Å) in the sequence $a^0a^0a^0 \rightarrow a^0b\ b^+ \rightarrow a^+a\ a^+ \rightarrow a\ a^+a$ (see Tables S3-S7).

To detail how the chemical identity of B impacts deformations within its first coordination sphere, we calculated the length-distortion parameter (ζ), expressed as $\zeta_k^j = \sum_{i=1}^{6} \left| d_{i,k} \quad d_{\mathrm{avg},k} \right|$ [74,75]. Here, $d_{i,k}$ is the i-th neareast neighbor B - I distance associated with the k-th BI_6 octahedron (B = Sn or Pb) in the j-th cluster expanding the alloy, while $d_{\mathrm{avg},k}$ is the average value of $d_{i,k}$ in the k-th octahedron. For each j containing N octahedrons in the SC, we computed the average value through $\overline{\zeta}^j = \sum_{k=1}^{N} \zeta_k^j / N$, making the GQCA averages ($\overline{\zeta}$) over $\overline{\zeta}^j$ through Equation (7) at 300 K, as plotted in Fig. 4.

For the $a^0a^0a^0$ polymorph, $\overline{\zeta}$ values reveal the PbI_6 octahedra are more distorted at lower Sn contents, which arises from the mismatch in radii between Sn and Pb cations. Nevertheless, this effect becomes balanced at $x \approx 0.50$, where the PbI_6 and SnI_6 octahedra exhibit nearly equal distortion. At this composition, the distortion trends are reversed, with SnI_6 becoming more distorted than PbI_6. Thus, since this polymorph does not show octahedral rotations, the primary factor influencing the B off-center displacements in the alloy is the disparity in cation sizes. This is particularly significant because in pristine $CsBI_3$ materials, this structural motif is absent. Consequently, even in this high-symmetry alloy, structural motifs with low symmetry regarding the $Pm\bar{3}m$ space group would be expected, revealing the mechanism of B-cation mixing as an additional factor contributing to the complex structural polymorphism observed in MHP-based materials.

The data presented in panels (b) and (c) allow to differentiate the effect of in-phase/out-of-phase rotations on the distortion of BI_6 octahedra. It is evident that the out-of-phase rotations around the b-axis lead to more platonic octahedra compared to their in-phase counterparts, i.e. $\overline{\zeta}(a^0b\ b^+) < \overline{\zeta}(a^0b^+b^+)$. Furthermore, the SnI_6 octahedra are even more affected by the $a^0b^+b^+$ Glazer's patterns, exhibiting approximately 59 % more distortion than their Pb-based counterparts in the $0.10 < x < 0.90$ compositions range. Since Sn can express stereochemically active ns^2 lone pairs in MHPs [76–78], the orientation of these pairs would tend to result in lesser octahedral distortions when out-of-phase rotations are present. When compared to $a^0a^0a^0$ in panel (a), $a^0b^{+(\ )}b^+$ Glazer's patterns show distortions even in the $CsBI_3$ pure MHPs. This observation

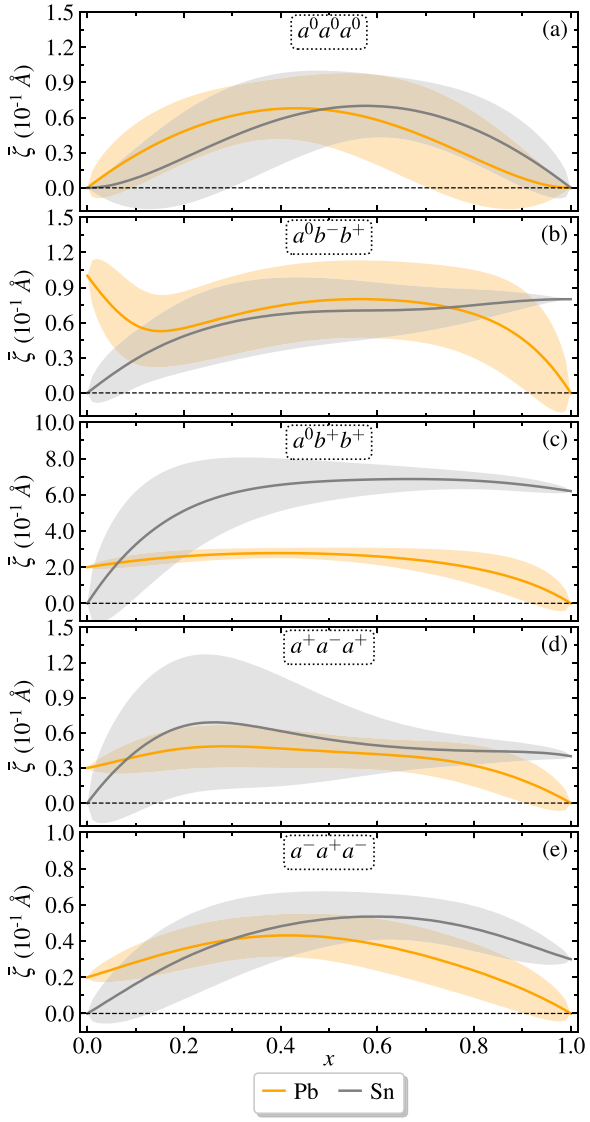

Fig. 4. Length-distortion parameter averaged over all BI_6 octahedrons ($\overline{\zeta}$), calculated at 300 K for (a) $\boldsymbol{a^0a^0a^0}$, (b) $\boldsymbol{a^0b^-b^+}$, (c) $\boldsymbol{a^0b^+b^+}$, (d) $\boldsymbol{a^+a^-a^+}$, and (e) $\boldsymbol{a^-a^+a^-}$ polymorphs of the $CsPb_{1-x}Sn_xI_3$ alloy.

underscores the role of such rotations in controlling the transition from platonic to distorted geometry for the octahedra in MHPs, which can directly impact their thermodynamic stability, as discussed below.

When analyzing the polymorphs with rotations around all three SC axes, i.e. $a^+a\ a^+$ and $a\ a^+a$, we verify that the presence of a third rotation axis consistently exerts a suppressive effect on the octahedral distortion in comparison with the $a^0b^{+(\ )}b^+$. However, panel (e) reveals that when two out-of-phase rotations occur in the $a\ a^+a$ configuration, they distort the PbI_6 octahedrons more significantly than SnI_6 only when $x < 0.30$. In the $a^+a\ a^+$ polymorph, two a^+ rotations always culminate in $\overline{\zeta}_{SnI_6} > \overline{\zeta}_{PbI_6}$ for $x > 0.10$, which confirms the earlier analysis indicating that in-phase rotations favor SnI_6 distortions over those of PbI_6.

3.2. Thermodynamic and Phase Stability

Energetic favorability of mixing $CsPbI_3$ and $CsSnI_3$ was quantified by calculating the $\Delta U(x, T)$ values for each polymorph using Equation (2). The results are shown in Fig. 5, with the respective clusters' excess energies presented as unfilled symbols.

In $a^0a^0a^0$ isostructural limit of alloy, most *js* configurations presented positive excess energies, indicating that mixing between $CsSnI_3$ and $CsPbI_3$ to form a highly symmetric alloy is usually unfavorable at low T. Indeed, at $x = 0.5\Delta\varepsilon_j < 0$ was observed, indicating a tendency for alloy's ordering in the ABBABAAB configuration. In this configuration, stability is achieved with SnI_6 and PbI_6 octahedra being intercalated, as represented in Figure S5. This ordering is expected to persist up to temperatures about 40 K, above which an alloy with B-sites randomly occupied is expected, as supported by the KL divergence in Figure S6. Similar findings are verified for the $a^0b^+b^+$ polymorph near $x = 0.10$. Still, the maximum KL value at $T = 0$ K indicates that the probability distribution from GQCA differs to a lesser extent from the distribution corresponding to a random alloy in comparison with $a^0a^0a^0$ at $x = 0.50$.

Interestingly, all isostructural polymorphs with at least two Glazer's rotations present $\Delta\varepsilon_j < 0$ at $x = 0.125$ for AAAAAAAB ordering (Figure S5), with values ranging between 0.17 and 20.60 mev/cation. This indicates that, in the presence of octahedral rotations, stability is achieved with the Sn cation being fully embedded in a matrix rich in Pb, thereby mitigating the initial strain caused by the incorporation of smaller Sn into the BI_3 sublattice.

Describing the thermodynamic MHP alloys only based on their isostructural Glazer's pattern is limiting. When considering all polymorphs forming a single ensemble in Fig. 5 (f), i.e. the APD statistics, we found that as T increases from 100–800 K, even the pristine $CsBI_3$ compounds began to have more polymorphic degrees of freedom in their ionic networks, with the $a^0a^0a^0$ contributions increasing at the higher energies. Among the polymorphs analyzed here, Fig. 6 shows that the one contributing most to $CsBI_3$ pristine compounds at room temperature ($T = 300$ K) is $a\ a^+a$, with the probabilities of $a^0a^0a^0$ ranging from 0.05 to 0.20 only when T is about 800 K.

Under conditions of constant pressure and temperature, the stability of $CsPb_{1-x}Sn_xI_3$ against phase segregation is analyzed through its free energy of mixing. In addition to energetic contribution described above, important configurational entropy effects are also considered (Equation (1)). The results obtained from GQCA approach for APD are presented in Fig. 7. Here, ΔF values are reported regarding the stablest polymorphic contribution from the $CsBI_3$ pristine MHPs, i.e. $a\ a^+a$. Discussions about the ΔF profiles calculated for isostructural Glazer's polymorphs, although they are limited, can be found in the Supporting Information (Figure S7), with the corresponding entropic contributions available in Figure S8.

Following the convex hull formalism [79–82], ΔF profiles in Fig. 7 evidence a favorable mixing of $CsPbI_3$ and $CsSnI_3$ compounds in the 100 K $< T <$ 800 K temperatures range since all curves are below the straight line connecting these compounds in their metastable structures at $T > 0$ K. In addition, these metastable structures change differently for Sn and Pb-based pristine MHPs, because of higher differences in $\Delta\varepsilon_j$ between $CsPbI_3$ polymorphs in comparison with $CsSnI_3$ ones (Fig. 5 ((e)).

To verify how polymorphic contributions affect the stability and metastability of $CsPb_{1-x}Sn_xI_3$ against phase segregation as a function of composition and temperature, we computed their *T*-*x* phase diagrams from the respective free energy profiles, as exhibited in Fig. 8. In isostructural limit, where the alloy presents only one Glazer's pattern regarding its BI_3 sublattice, we found critical temperatures usually in the range of 20–38 K, except for $a^0b\ b^+$ presenting $T_c \approx 330$ K. Above T_c, the alloy is stable as a solid solution for all x values, while below it, phase segregation is thermodynamically favored within the region enclosed by the binodal line [41].

When octahedral rotations are absent in the BI_3 sublattice, i.e. the alloy is configured as $a^0a^0a^0$, panel (a) reveals the presence of two miscibility gaps around $x = 0.50$, located between $0.02 < x < 0.44$ and $0.53 < x < 0.97$ at $T = 20$ K, respectively. At $x = 0.50$, $a^0a^0a^0$ alloy would tend to order in an ABBABAAB pattern when T is reduced, in accordance with Figures S6 and S9 in Supporting Information. However, since the clusters associated with this polymorph contribute less pronouncedly to properties of the alloy when APD is considered (Fig. 6), it does not reflect the phase diagram that would be verified experimentally when considering polymorphic features of MHPs alloys.

Meanwhile the alloy presents octahedral rotations only along [010] and [001] directions – which is represented by the $a^0b\ b^+$ and $a^0b^+b^+$ polymorphs – the preference for ABBABAAB ordering at $x = 0.50$ is lost, with this composition situated within the miscibility gap regions in panels (b) and (c). Interestingly $a^0b\ b^+$ shows a higher T_c in comparison with $a^0b^+b^+$, although the former has $\Delta U < 0$ for a larger range of compositions. Despite many alloys do not present miscibility gaps when $\Delta U < 0$, phase segregation can occur [83]. So, in spite of $\Delta U > 0$ being found for $a^0b^+b^+$ polymorph in the range $0.20 < x < 1.00$, its $\Delta\varepsilon_j > 0$ present smaller magnitudes in comparison with $a^0b\ b^+$ ones. When the temperature is raised, the entropic effects dominate over the energetic ones for $a^0b^+b^+$, leading to a lower T_c value. For $a^0b\ b^+$, the x_j's associated with $\Delta\varepsilon_j > 0$ increase following 5 K → 800 K (Figure S10), which acts as a driving force for phase segregation, increasing T_c and competing with the stabilization provided by ΔS contributions.

If octahedral rotations are also presented around the [100] direction – represented by the $a\ a^+a$ and $a^+a\ a^+$ polymorphs – panel (d) exposes the opposite effect of in-phase/out-of-phase rotation in stabilization/destabilization of the alloy in comparison with the two directions rotations in the $a^0b\ b^+$ configuration. For $a^+a\ a^+$, the more significant number of *js* with $\Delta\varepsilon_j < 0$ (Fig. 5 (d)) contributes to the energy stabilization of the alloy and, thus, no miscibility gap was found for this system for the temperatures range considered. As for the $a\ a^+a$ polymorph, although most *js* present $\Delta\varepsilon_j > 0$ (Fig. 5 (e)), their magnitudes are smaller than those in $a^0b\ b^+$ and, thus, the entropic effects dominate faster over the energetic ones, resulting in a smaller T_c in panel (d) compared to that presented in panel (b).

The effect of considering APD on the phase stability of $CsPb_{1-x}Sn_xI_3$ is shown in Fig. 8 (e), which shows a stable solid solution for the entire temperature range only for $0.00 < x < 0.10$. Compared with isostructural polymorphs, there is an enlargement of unstable green region, revealing that cooperation between all polymorphs described above favors phase segregation for $x > 0.10$ when $T < T_c$. However, since T_c is relatively low, the phase segregation tendency at room temperature – which would be present in the alloy with a single $a^0b\ b^+$ pattern – is mitigated, suggesting that $CsPb_{1-x}Sn_xI_3$ alloy remains a stable solid solution against phase segregation even at $T \geqslant 300$ K for solar cells applications.

3.3. Polymorphic effects on the gap energy

The electronic behavior of $CsPb_{1-x}Sn_xI_3$ was analyzed by computing the GQCA average of E_g over a range of compositions for APD. The

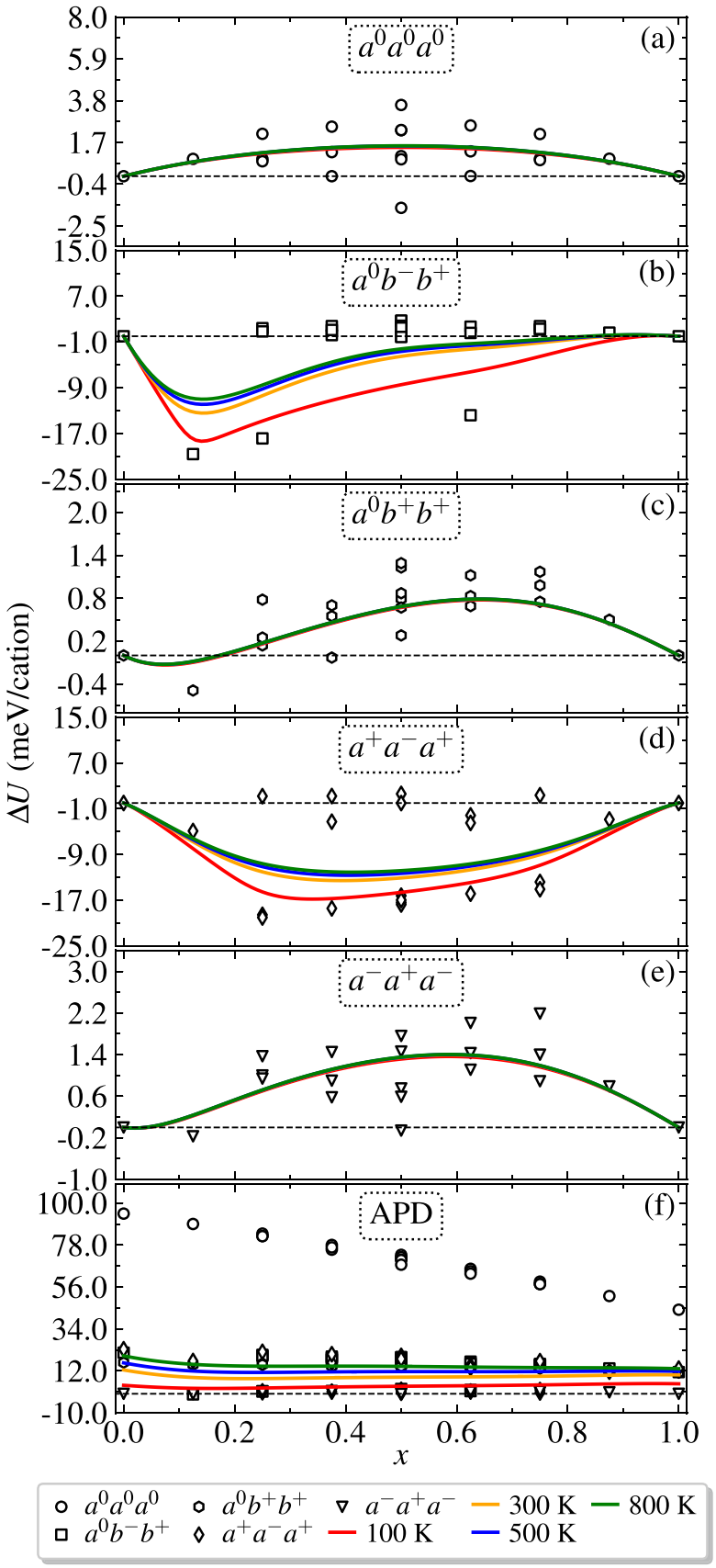

Fig. 5. Excess energy (scatter) and mixing internal energies (ΔU) calculated as a function of composition (x) at several temperatures in range of 100 K to 800 K for (a) $\boldsymbol{a^0a^0a^0}$, (b) $\boldsymbol{a^0b^-b^+}$, (c) $\boldsymbol{a^0b^+b^+}$, (d) $\boldsymbol{a^+a^-a^+}$, (e) $\boldsymbol{a^-a^+a^-}$ polymorphs, and (f) by considering all polymorphic degrees (APD) of the $CsPb_{1-x}Sn_xI_3$ alloy.

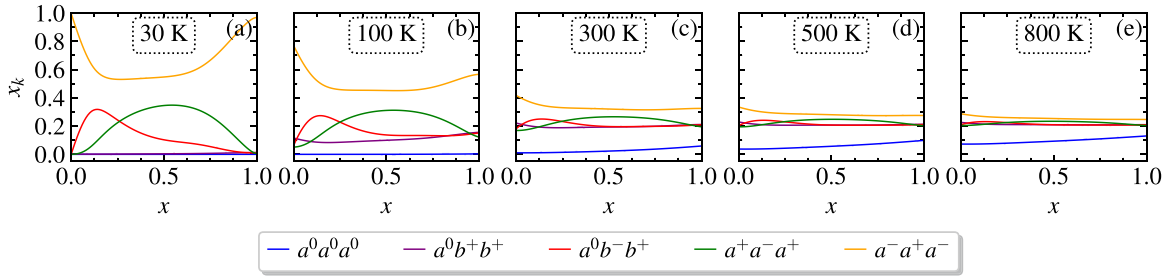

Fig. 6. Polymorph probabilities (x_k) as a function of composition, calculated at (a) 30 K, (b) 100 K, (c) 300 K, (d) 500 K, and (e) 800 K by considering the APD statistics.

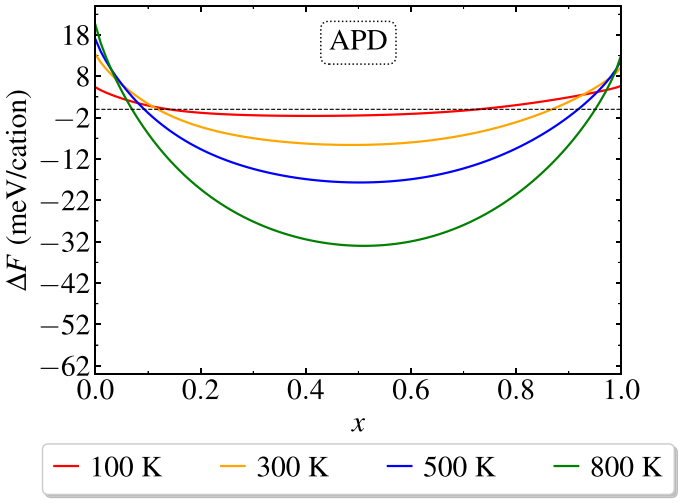

Fig. 7. Mixing free energies (ΔF) calculated as a function of composition at several temperatures ranging from 100–800 K by considering all polymorphic degrees (APD) of the $CsPb_{1-x}Sn_xI_3$ alloy.

results, obtained through the DFT-1/2+SOC and DFT protocols, are shown in Fig. 9 (a). The E_g values obtained using DFT combined with SOC (DFT+SOC) can be accessed in Figure S11, while the numerical E_g values for all *js* expanding the alloy are available in Tables S8-S12, which were direct regarding the **k**-point in the reciprocal space.

According to Fig. 9 (a), DFT protocol leads to a quasi-linear dependence of E_g over x, with gap energy values for $CsPbI_3$ ($CsSnI_3$) being overestimated (underestimated) by about 6.9 % (35.7 %) regarding the experimental references. This indicates that such a protocol is not sufficient to investigate the dependence of the alloy's gap energies on the alloy's composition. This discrepancy is consistent with previous studies we carried out on the properties of the polymorphous pure MHPs that form the $CsPb_{1-x}Sn_xI_3$ system investigated here [32,33]. The presence of heavy elements such as Pb, Sn, and I in MHPs causes pronounced relativistic effects on their corresponding electronic structures, which cannot be neglected when comparing calculated and experimentally measured data [29,31,85–87]. This is further confirmed by the GQCA curve obtained via DFT-1/2+SOC procol in panel (a), in which we found the calculated E_g values in excellent agreement with experimental ones, falling within the statistical errors calculated via the GQCA APD ensemble for the cubic alloy.

The GQCA curve calculated via DFT-1/2+SOC protocol in panel (a) reveals a non-linear dependence of E_g over x, known as bandgap bowing

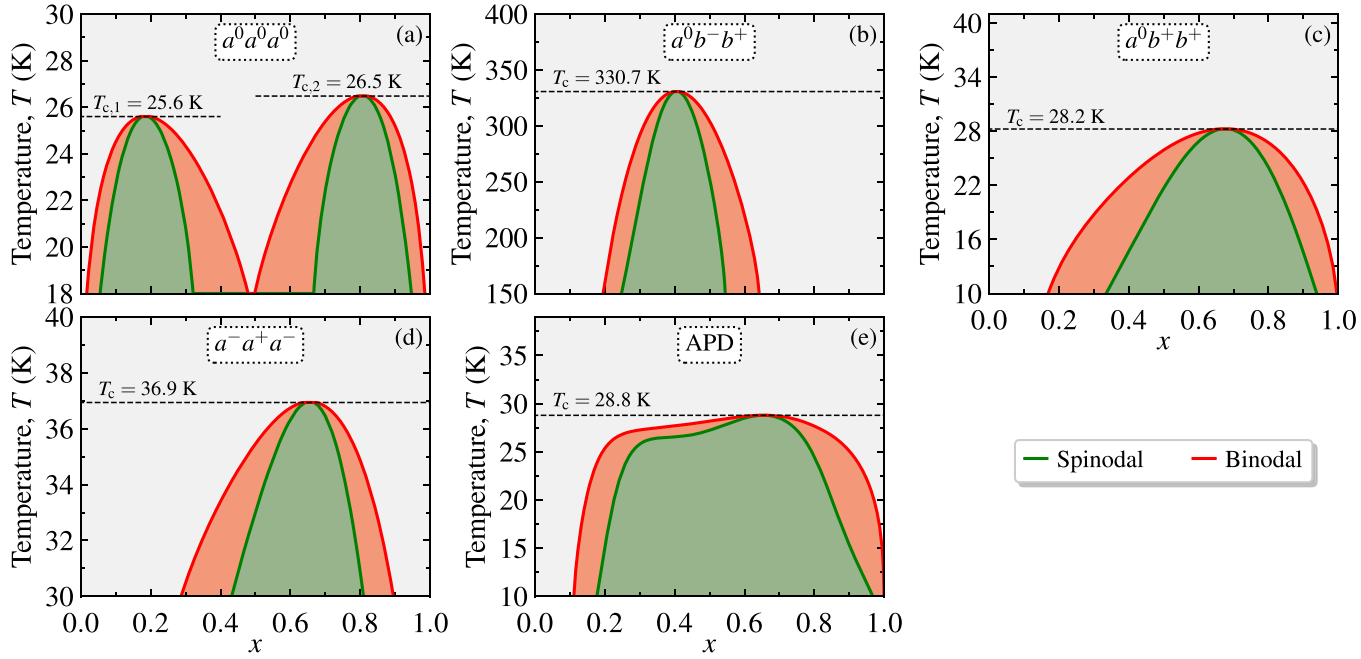

Fig. 8. Phase diagrams calculated as a function of composition (x) and temperature (T) for the $CsPb_{1-x}Sn_xI_3$ alloy in the (a) $\boldsymbol{a}^0\boldsymbol{a}^0\boldsymbol{a}^0$, (b) $\boldsymbol{a}^0\boldsymbol{b}^-\boldsymbol{b}^+$, (c) $\boldsymbol{a}^0\boldsymbol{b}^+\boldsymbol{b}^+$, (d) $\boldsymbol{a}^-\boldsymbol{a}^+\boldsymbol{a}^-$, and (e) APD polymorphs. The spinodal regions are depicted in green, while the metastable ones are shown in red. In the gray region, the solid solution is stable against phase segregation. Dashed lines indicate the critical temperatures (T_c).

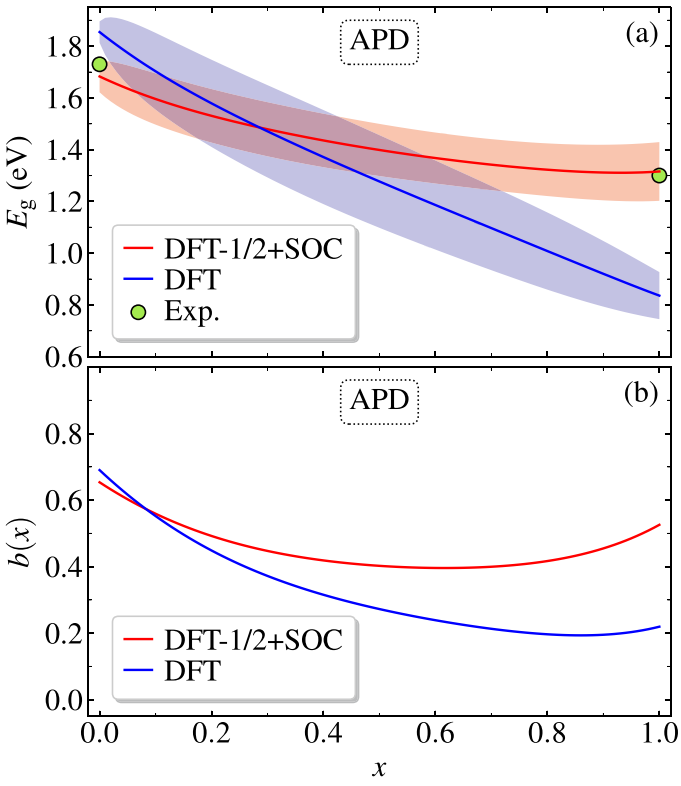

Fig. 9. (a) Gap energies (E_g) calculated as a function of composition at room temperature (300 K) by considering all polymorphic degrees (APD) of the $CsPb_{1-x}Sn_xI_3$ alloy. Experimental references, when available, are shown as unifilled symbols and were taken from references: [10] ($CsPbI_3$) and [84] ($CsSnI_3$). (b) Bowing parameter ($b(x)$) calculated as a function of composition at room temperature through DFT (blue) and DFT-1/2+SOC (red) protocols.

[29,88,89]. To quantify this effect, we considered the pseudo-parabolic expression $E_g(x) = (1 \quad x)E_g(CsPbI_3) + xE_g(CsSnI_3) + b(x)x(1 \quad x)$ [90], where the bowing parameter b depends on the Sn content in the alloy, representing an advancement over the constant b approach [91]. The complete $b \quad x$ dependence is presented in Fig. 9 (b). The same curve calculated using the DFT protocol is also shown for comparison.

For compositions $x > 0.10$, the bowing parameter curve in panel (b) obtained via the DFT-1/2+SOC protocol shows higher b values than those computed with DFT only. The latter is a result of a nearly non-linear profile of E_g as a function of x, which is caused by structural changes in the material as x varies from 0.0 to 1.0 through the polymorphic contributions discussed in the structural analysis section. From Figure S11 (a,b), it can be observed that including SOC leads to a similar profile for the gap energies and the corresponding bowing parameter curve. However, the quasiparticle correction DFT-1/2 is essential for ensuring that the calculated values are comparable with their experimental references. This is because only the SOC inclusion in the DFT+SOC protocol culminates in considerably underestimated E_g values within a slightly flatter $b(x)$ dependence. This discrepancy is pronounced for $CsSnI_3$ in comparison with $CsPbI_3$ since there is a fortuitous error cancellation due to the stronger relativistic effects related to Pb [29]. This shows the relevance of using a complete protocol that includes all necessary relativistic corrections plus polymorphic features for MHPs electronic structure calculation protocols, which culminates in an excellent agreement between calculated and the corresponding experimental reports.

3.4. PCE from SLME model combined with GQCA

The combination of the SLME model with the DFT-1/2+SOC, allowed us to calculate the PCE values for $CsPb_{1\ x}Sn_xI_3$ alloy at $T =$ 300 K within the GQCA APD statistics. These results are presented in Fig. 10, while the absorption coefficient calculated at $x = 0.45$, corresponding to the minimum of $\Delta F(x,\ 300\ K)$ in a convex hull-like perspective, is available in Figure S12. PCE values calculated for other temperatures (100 K, 500 K, 800 K) can be found in Figure S13.

The curve in Fig. 10 reveals that the PCE values computed for $CsPb_{1\ x}Sn_xI_3$ generally follow the E_g tendencies presented in Fig. 9 (a), i. e. lower gap energies are related to higher PCEs. However, the highest PCE (30.72 %) occurs for $x = 1.00$, corresponding to pure $CsSnI_3$ MHP, rather than $x = 0.93$, which corresponds to the lowest $E_g = 1.31$ eV. To attain a complete overview of this, in Fig. 11, we correlated the APD gap energies and total absorbance as a function of composition at 300 K. This analysis reveals that the higher PCE of $CsSnI_3$ in comparison with $CsPb_{0.07}Sn_{0.93}I_3$ arises from a compensatory effect between E_g and $\sum\alpha$, since $CsSnI_3$ gap energy is only slightly larger (1.32 eV), while its total absorbance (17.90×10^6 cm ^{1}) is greater than that of $CsPb_{0.07}Sn_{0.93}I_3$ (17.54×10^6 cm ^{1}). Nonetheless, since the pristine tin-based MHP is more prone to oxidation in air than their Pb-based relative [92–94], the use of alloy could reduce this tendency while increasing the sought-after long-term stability of photovoltaic devices [44,95,96]. However, this must be done in a balanced way, since toxic lead halides are generally considered potential carcinogens, and excess Pb could cause future dismantling of such lead-based MHPs in the solar cells market [97–99]. Nonetheless, since there is no miscibility gap at $T \geq 30$ K for the studied APD alloy (Fig. 8), $CsPb_{1\ x}Sn_xI_3$ emerges as a thermodynamically stable candidate for solar cell applications across a wide range of operational conditions compared to its hybrid analog, whose predicted $T_c = 204$ K by a similar protocol used here would be considerably higher [28].

4. Conclusion

We conducted first-principles calculations combined with a statistical approach based on the generalized quasichemical approximation to study the impact of polymorphic features on the electronic properties and thermodynamic stability of $CsPb_{1\ x}Sn_xI_3$ alloys. We found that while the alloy's lattice parameter closely adheres to Vegard's law, in-phase octahedron rotations tend to distort SnI_6 ones at the expense of PbI_6 octahedrons, which is correlated with the presence of a stereochemically active ns^2 electronic pair in Sn. Thus, we showed the importance of polymorphic features in stabilizing the alloy under solar cells operational conditions, with $a^0a^0a^0$ polymorph contributing minimally compared to the dominant $a \quad a^+a$ configuration. The inclusion of all polymorphic degrees in the APD generalized ensemble led to an

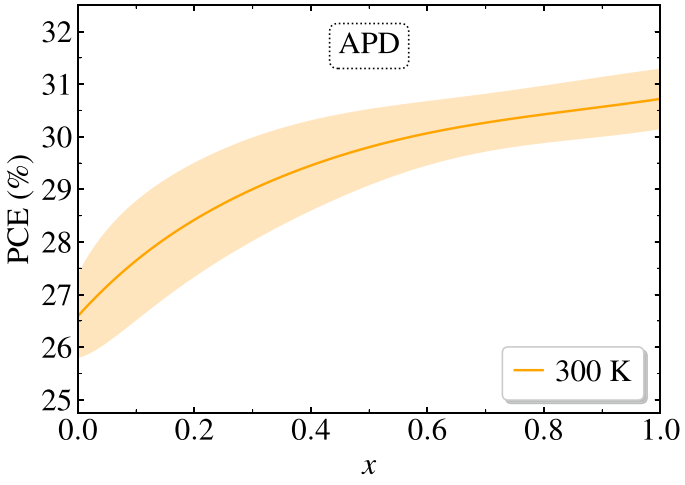

Fig. 10. Calculated power conversion efficiency (PCE) for $CsPb_{1-x}Sn_xI_3$ through APD GQCA statistics via the SLME model, considering the alloy thickness as 1 μm and $T \quad$ 300 K.

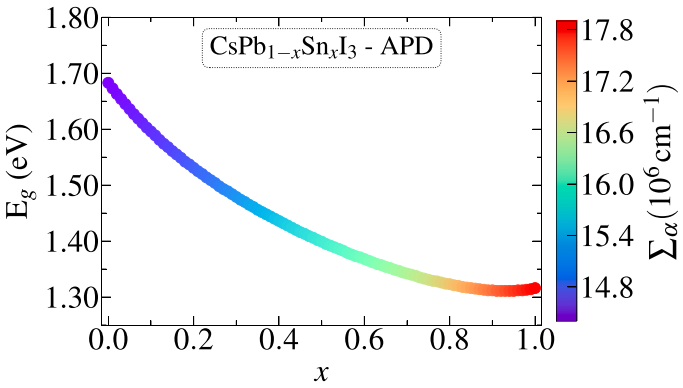

Fig. 11. Correlation between the gap energy, composition, and total absorption coefficient ($\sum_\alpha$) calculated for $CsPb_{1-x}Sn_xI_3$ through APD GQCA statistics at 300 K. The color map corresponds to the $\sum_\alpha$ obtained via GQCA for the photon energy range 0.0–4.0 eV.

expanded phase-segregation favored region in the respective T x phase diagram, which is compensated by a considerably small critical temperature evaluated as only 28.8 K. Consequently, despite the slightly lower PCE of the alloys compared to $CsSnI_3$ according to the SLME model, the presence of Pb could mitigate the tendency of Sn-based MHPs to oxidize in air, favoring the fabrication of long-term stable photovoltaic devices. In addition, the all-inorganic $CsPb_{1\ x}Sn_xI_3$ system proved to be a more promising candidate for this application than its hybrid analog, given its considerably lower critical temperature. This characteristic enhances its suitability for use in very low-temperature conditions, broadening the operational range of the device and reducing the risk of instability due to phase segregation and resultant property degradation. Consequently, these advantages could drive market adoption of solar cells based on this material for deployment in both extremely hot and extremely cold regions of Earth.

CRediT authorship contribution statement

Wolfgang Wenzel: Writing – review & editing, Writing – original draft, Visualization, Validation, Resources, Investigation, Formal analysis. **Carlos Maciel de Oliveira Bastos:** Writing – review & editing, Writing – original draft, Validation, Software, Methodology, Investigation, Formal analysis. **Maurício J. Piotrowski:** Writing – review & editing, Writing – original draft, Visualization, Validation, Software, Methodology, Investigation, Formal analysis. **Dias C. Alexandre:** Writing – review & editing, Writing – original draft, Validation, Software, Methodology, Investigation, Formal analysis. **Diego Guedes-Sobrinho:** Writing – review & editing, Writing – original draft, Validation, Supervision, Software, Resources, Project administration, Methodology, Investigation, Funding acquisition, Formal analysis, Conceptualization. **Luis Octavio de Araujo:** Writing – review & editing, Writing – original draft, Visualization, Validation, Software, Methodology, Investigation, Formal analysis. **Celso R. C. Rêgo:** Writing – review & editing, Writing – original draft, Validation, Supervision, Methodology, Investigation, Formal analysis.

Declaration of Competing Interest

The authors declare that they have no known competing financial interests or personal relationships that could have appeared to influence the work reported in this paper.

Data availability

Data will be made available on request.

Acknowledgements

The authors thank the Atos and Ogun Computer at CIMATEC SENAI (Salvador – BA) and "Laboratório Central de Processamento de Alto Desempenho" (LCPAD) financed by FINEP through CT-INFRA/UFPR projects, both in Brazil for the support to perform the electronic structure calculations. The authors gratefully acknowledge the Karlsruhe Institute of Technology (KIT) for the HoreKa super computer resources. L.O.A. thanks the Coordination for Improvement of Higher Level Education CAPES (finance Code 001) for funding. The authors are also thankful for financial support from the National Council for Scientific and Technological Development (CNPq, grant numbers 307345/2021-1, 408144/2022-0, 313081/2017-4 and 305335/2020-0), Federal District Research Support Foundation (FAPDF, grants 00193-00001817/2023-43 and 00193-00002073/2023-84), the Coordination for Improvement of Higher Level Education (CAPES), the Rio Grande do Sul Research Foundation (FAPERGS). In addition, the authors thanks the "Centro Nacional de Processamento de Alto Desempenho em São Paulo" (CENAPAD-SP, UNICAMP/FINEP - MCTI project) for resources into the 897 and 570 projects, Lobo Carneiro HPC (NACAD) at the Federal University of Rio de Janeiro (UFRJ) for resources (133 projects). W.W. and C.R.C.R. thank the German Federal Ministry of Education and Research (BMBF) for financial support of the project Innovation-Platform MaterialDigital (www.materialdigital.de) through project funding FKZ number 13XP5094A.

References

[1] A. Kojima, K. Teshima, Y. Shirai, T. Miyasaka, Organometal halide perovskites as visible-light sensitizers for photovoltaic cells, J. Am. Chem. Soc. 131 (17) (2009) 6050–6051, https://doi.org/10.1021/ja809598r.
[2] A.K. Jena, A. Kulkarni, T. Miyasaka, Halide perovskite photovoltaics: background, status, and future prospects, Chem. Rev. 119 (5) (2019) 3036–3103, https://doi.org/10.1021/acs.chemrev.8b00539.
[3] J. Park, J. Kim, H.-S. Yun, M.J. Paik, E. Noh, H.J. Mun, M.G. Kim, T.J. Shin, S. I. Seok, Controlled growth of perovskite layers with volatile alkylammonium chlorides, Nature 616 (7958) (2023) 724–730, https://doi.org/10.1038/s41586-023-05825-y.
[4] S.V. Trukhanov, I.O. Troyanchuk, M. Hervieu, H. Szymczak, K. Bärner, Magnetic and electrical properties of $LBaMn_2O_{6-\gamma}$ (L= Nd, Sm, Eu, Gd, Tb) manganites, Phys. Rev. B 66 (18) (2002) 184424, https://doi.org/10.1103/physrevb.66.184424.
[5] M.A. Green, E.D. Dunlop, M. Yoshita, N. Kopidakis, K. Bothe, G. Siefer, X. Hao, Solar cell efficiency tables (version 62), Prog. Photovolt. Res. Appl. 31 (7) (2023) 651–663, https://doi.org/10.1002/pip.3726.
[6] M.A. Green, E.D. Dunlop, M. Yoshita, N. Kopidakis, K. Bothe, G. Siefer, X. Hao, Solar cell efficiency tables (version 63), Prog. Photovolt. Res. Appl. 32 (1) (2023) 3–13, https://doi.org/10.1002/pip.3750.
[7] B.R. Bade, K.B. Kore, S.R. Rondiya, D.S. Nilegave, M.P. Nasane, S.B. Jathar, S. V. Barma, S.R. Jadkar, A.M. Funde, Room TEmperature Synthesis of Formamidinium Lead Iodide ($FAPbI_3$) perovskite for low-cost absorber in solar cells, ES Energy Environ. 13 (1) (2021) 31–36.
[8] E.J. Juarez-Perez, Z. Hawash, S.R. Raga, L.K. Ono, Y. Qi, Thermal degradation of $CH_3\ NH_3\ PbI_3$ perovskite into NH_3 and CH_3 I gases observed by coupled thermogravimetry-mass spectrometry analysis, Energy Environ. Sci. 9 (11) (2016) 3406–3410, https://doi.org/10.1039/c6ee02016j.
[9] E. Aktas, N. Rajamanickam, J. Pascual, S. Hu, M.H. Aldamasy, D. DiGirolamo, W. Li, G. Nasti, E. Martínez-Ferrero, A. Wakamiya, E. Palomares, A. Abate, Challenges and strategies toward long-term stability of lead-free tin-based perovskite solar cells, Commun. Mater. 3 (1) (2022) 104, https://doi.org/10.1038/s43246-022-00327-2.
[10] E.M. Sanehira, A.R. Marshall, J.A. Christians, S.P. Harvey, P.N. Ciesielski, L. M. Wheeler, P. Schulz, L.Y. Lin, M.C. Beard, J.M. Luther, Enhanced mobility $CsPbI_3$ quantum dot arrays for record-efficiency, high-voltage photovoltaic cells, Sci. Adv. 3 (10) (2017) eaao4204, https://doi.org/10.1126/sciadv.aao4204.
[11] Z. Chen, L. Dong, H. Tang, Y. Yu, L. Ye, J. Zang, Direct synthesis of cubic phase $CsPbI_3$ nanowires, CrystEngComm 21 (9) (2019) 1389–1396, https://doi.org/10.1039/C8CE02111B.
[12] K. Gesi, K. Ozawa, S. Hirotsu, Effect of hydrostatic pressure on the structural phase transitions in $CsPbCl_3$ and $CsPbBr_3$, J. Phys. Soc. Jpn. 38 (2) (1975) 463–466, https://doi.org/10.1143/jpsj.38.463.

[13] B.R. Sutherland, Solar materials find their band gap, Joule 4 (5) (2020) 984–985, https://doi.org/10.1016/j.joule.2020.05.001.

[14] G.E. Eperon, G.M. Paternò, R.J. Sutton, A. Zampetti, A.A. Haghighirad, F. Cacialli, H.J. Snaith, Inorganic caesium lead iodide perovskite solar cells, J. Mater. Chem. A 3 (39) (2015) 19688–19695, https://doi.org/10.1039/C5TA06398A.

[15] A. Bonadio, C.A. Escanhoela, F.P. Sabino, G. Sombrio, V.G. de Paula, F.F. Ferreira, A. Janotti, G.M. Dalpian, J.A. Souza, Entropy-driven stabilization of the cubic phase of $MAPbI_3$ at room temperature, J. Mater. Chem. A 9 (2) (2021) 1089–1099, https://doi.org/10.1039/D0TA10492B.

[16] A. Swarnkar, W.J. Mir, A. Nag, Can B-site doping or alloying improve thermal- and phase-stability of all-inorganic $CsPbX_3$ (X = Cl, Br, I) perovskites, ACS Energy Lett. 3 (2) (2018) 286–289, https://doi.org/10.1021/acsenergylett.7b01197.

[17] M.I. Ustinova, M.M. Mikheeva, G.V. Shilov, N.N. Dremova, L. Frolova, K. J. Stevenson, S.M. Aldoshin, P.A. Troshin, Partial substitution of Pb^{2+} in $CsPbI_3$ as an efficient strategy to design fairly stable all-inorganic perovskite formulations, ACS Appl. Mater. Interfaces 13 (4) (2021) 5184–5194, https://doi.org/10.1021/acsami.0c18061.

[18] C.-H. Lu, G.V. Biesold-McGee, Y. Liu, Z. Kang, Z. Lin, Doping and ion substitution in colloidal metal halide perovskite nanocrystals, Chem. Soc. Rev. 49 (14) (2020) 4953–5007, https://doi.org/10.1039/c9cs00790c.

[19] A. Dehingia, U. Das, A. Roy, Compositional engineering in α -$CsPbI_3$ toward the efficiency and stability enhancement of all inorganic perovskite solar cells, ACS Appl. Energy Mater. 5 (10) (2022) 12099–12108, https://doi.org/10.1021/acsaem.2c01543.

[20] K.T. Jacob, S. Raj, L. Rannesh, Vegard's law: a fundamental relation or an approximation, Int. J. Mater. Res. 98 (9) (2007) 776–779, https://doi.org/10.3139/146.101545.

[21] M. Becker, T. Klüner, M. Wark, Formation of hybrid ABX_3 perovskite compounds for solar cell application: first-principles calculations of effective ionic radii and determination of tolerance factors, Dalton Trans. 46 (11) (2017) 3500–3509, https://doi.org/10.1039/c6dt04796c.

[22] A. Swarnkar, A.R. Marshall, E.M. Sanehira, B.D. Chernomordik, D.T. Moore, J. A. Christians, T. Chakrabarti, J.M. Luther, Quantum dot-induced phase stabilization of α -$CsPbI_3$ perovskite for high-efficiency photovoltaics, Science 354 (6308) (2016) 92–95, https://doi.org/10.1126/science.aag2700.

[23] K.M. Sim, A. Swarnkar, A. Nag, D.S. Chung, Phase stabilized α -$CsPbI_3$ perovskite nanocrystals for photodiode applications, Laser Photonics Rev. 12 (1) (2017) 1700209, https://doi.org/10.1002/lpor.201700209.

[24] R.M.I. Bandara, S.M. Silva, C.C.L. Underwood, K.D.G.I. Jayawardena, R.A. Sporea, S.R.P. Silva, Progress of Pb-Sn mixed perovskites for photovoltaics: a review, Energy Environ. Mater. 5 (2) (2021) 370–400, https://doi.org/10.1002/eem2.12211.

[25] F. Cao, J. Chen, D. Yu, S. Wang, X. Xu, J. Liu, Z. Han, B. Huang, Y. Gu, K.L. Choy, H. Zeng, Bionic detectors based on low-bandgap inorganic perovskite for selective NIR-I photon detection and imaging, Adv. Mater. 32 (6) (2019) 1905362, https://doi.org/10.1002/adma.201905362.

[26] M. Anaya, G. Lozano, M.E. Calvo, H. Míguez, ABX3 perovskites for tandem solar cells, Joule 1 (4) (2017) 769–793, https://doi.org/10.1016/j.joule.2017.09.017.

[27] Q. Sun, Z. Zhang, T. Zhang, Y. Feng, A. Gu, H. Yu, M. Zhang, X.L. Zhang, J. Zhu, Y. Shen, M. Wang, Integrated 4-terminal all-inorganic perovskite tandem solar cell with open-circuit voltage exceeding 2.1 V for water splitting, ACS Energy Lett. 7 (12) (2022) 4215–4223, https://doi.org/10.1021/acsenergylett.2c02262.

[28] D. Guedes-Sobrinho, I. Guilhon, M. Marques, L.K. Teles, Thermodynamic stability and structural insights for $CH_3 NH_3 Pb_{1-x} Si_x I_3$, $CH_3 NH_3 Pb_{1-x} Ge_x I_3$, and $CH_3 NH_3 Pb_{1-x} Sn_x I_3$ hybrid perovskite alloys: a statistical approach from first principles calculations, Sci. Rep. 9 (1) (2019) 11061, https://doi.org/10.1038/s41598-019-47192-7.

[29] D. Guedes-Sobrinho, I. Guilhon, M. Marques, L.K. Teles, Relativistic DFT-1/2 calculations combined with a statistical approach for electronic and optical properties of mixed metal hybrid perovskites, J. Phys. Chem. Lett. 10 (15) (2019) 4245–4251, https://doi.org/10.1021/acs.jpclett.9b01499.

[30] X. Zhao, G.M. Dalpian, Z. Wang, A. Zunger, Polymorphous nature of cubic halide perovskites, Phys. Rev. B 101 (15) (2020) 155137, https://doi.org/10.1103/PhysRevB.101.155137.

[31] L.O. de Araujo, F.P. Sabino, C.R.C. Rêgo, D. Guedes-Sobrinho, Bulk Rashba effect splitting and suppression in polymorphs of metal iodine perovskites, J. Phys. Chem. Lett. 12 (30) (2021) 7245–7251, https://doi.org/10.1021/acs.jpclett.1c02048.

[32] L.O. de Araujo, C.R.C. Rêgo, W. Wenzel, F.P. Sabino, D. Guedes-Sobrinho, Impact of the polymorphism and relativistic effects on the electronic properties of inorganic metal halide perovskites, J. Phys. Chem. C. 126 (4) (2022) 2131–2140, https://doi.org/10.1021/acs.jpcc.1c08923.

[33] L.O. de Araujo, C.R.C. Rêgo, W. Wenzel, D.N. Silveira, M.J. Piotrowski, F.P. Sabino, Y. Pramudya, D. Guedes-Sobrinho, How cation nature controls the bandgap and bulk rashba splitting of halide perovskites, J. Comput. Chem. 44 (14) (2023) 1395–1403, https://doi.org/10.1002/jcc.27094.

[34] X.-G. Zhao, Z. Wang, O.I. Malyi, A. Zunger, Effect of static local distortions vs. dynamic motions on the stability and band gaps of cubic oxide and halide perovskites, Mater. Today 49 (2021) 107–122, https://doi.org/10.1016/j.mattod.2021.05.021.

[35] G.M. Dalpian, X. Zhao, L. Kazmerski, A. Zunger, Formation and composition-dependent properties of alloys of cubic halide perovskites, Chem. Mater. 31 (7) (2019) 2497–2506, https://doi.org/10.1021/acs.chemmater.8b05329.

[36] A.C. Dias, M.P. Lima, J.L.F. Da Silva, Role of structural phases and octahedra distortions in the optoelectronic and excitonic properties of $CsGeX_3$ (X = Cl, Br, I) perovskites, J. Phys. Chem. C. 125 (35) (2021) 19142–19155, https://doi.org/10.1021/acs.jpcc.1c05245.

[37] R.X. Yang, J.M. Skelton, E.L. daSilva, J.M. Frost, A. Walsh, Spontaneous octahedral tilting in the cubic inorganic cesium halide perovskites $CsSnX_3$ and $CsPbX_3$ (X = F, Cl, Br, I), J. Phys, Chem. Lett. 8 (19) (2017) 4720–4726, https://doi.org/10.1021/acs.jpclett.7b02423.

[38] A. Sher, M. van Schilfgaarde, A. Chen, W. Chen, Quasichemical approximation in binary alloys, Phys. Rev. B 36 (8) (1987) 4279–4295, https://doi.org/10.1103/PhysRevB.36.4279.

[39] S. Kadkhodaei, J.A. Muñoz, Cluster expansion of alloy theory: a review of historical development and modern innovations, JOM 73 (11) (2021) 3326–3346, https://doi.org/10.1007/s11837-021-04840-6.

[40] M. Moaddeli, M. Kanani, A. Grünebohm, Electronic and structural properties of mixed-cation hybrid perovskites studied using an efficient spin-orbit included DFT-1/2 approach, Phys. Chem. Chem. Phys. 25 (37) (2023) 25511–25525, https://doi.org/10.1039/d3cp02472e.

[41] L.K. Teles, J. Furthmüller, L.M.R. Scolfaro, J.R. Leite, F. Bechstedt, First-principles calculations of the thermodynamic and structural properties of strained $In_xGa_{1-x}N$ and $Al_xGa_{1-x}N$ Alloys, Phys. Rev. B 62 (4) (2000) 2475–2485, https://doi.org/10.1103/PhysRevB.62.2475.

[42] F. Brivio, C. Caetano, A. Walsh, Thermodynamic origin of photoinstability in the $CH_3 NH_3 Pb(I_{1-x} Br_x)_3$ hybrid halide perovskite alloy, J. Phys. Chem. Lett. 7 (6) (2016) 1083–1087, https://doi.org/10.1021/acs.jpclett.6b00226.

[43] P. Borlido, F. Bechstedt, S. Botti, C. Rödl, Ensemble averages of ab initio optical, transport, and thermoelectric properties of hexagonal $Si_x Ge_{1-x}$ alloys, Phys. Rev. Mater. 7 (1) (2023) 014602, https://doi.org/10.1103/PhysRevMaterials.7.014602.

[44] F. Valadares, I. Guilhon, L.K. Teles, M. Marques, Atomistic origins of enhanced band gap, miscibility, and oxidation resistance in α -$CsPb_{1-x}Sn_xI_3$ mixed perovskite, J. Phys. Chem. C. 124 (48) (2020) 26124–26133, https://doi.org/10.1021/acs.jpcc.0c07356.

[45] R.M. dos Santos, I. Ornelas-Cruz, A.C. Dias, M.P. Lima, J.L.F. Da Silva, Theoretical investigation of the role of mixed A^+ cations in the structure, stability, and electronic properties of perovskite alloys, ACS Appl. Energy Mater. 6 (10) (2023) 5259–5273, https://doi.org/10.1021/acsaem.3c00186.

[46] A.M. Glazer, The classification of tilted octahedra in perovskites, Acta Crystallogr., Sect. B: Struct. Crystallogr. Cryst. Chem. 28 (11) (1972) 3384–3392, https://doi.org/10.1107/S0567740872007976.

[47] A. Schleife, M. Eisenacher, C. Rödl, F. Fuchs, J. Furthmüller, F. Bechstedt, Ab Initio description of heterostructural alloys: thermodynamic and structural properties of $Mg_x Zn_{1-x} O$ and $Cd_x Zn_{1-x} O$, Phys. Rev. B 81 (24) (2010) 245210, https://doi.org/10.1103/PhysRevB.81.245210.

[48] S. Kullback, R.A. Leibler, On information and sufficiency, Ann. Math. Stat. 22 (1) (1951) 79–86, https://doi.org/10.1214/aoms/1177729694.

[49] J.W.D. Connolly, A.R. Williams, Density-functional theory applied to phase transformations in transition-metal alloys, Phys. Rev. B 27 (8) (1983) 5169–5172, https://doi.org/10.1103/physrevb.27.5169.

[50] H. Kittel, 1980, , Charles; Kroemer, Thermal Physics, 2nd Edition, W. H. Freeman.

[51] K. Binder, P. Fratzl, Spinodal Decomposition, Phase Transformations in Materials, John Wiley & Sons, Ltd, 2001, pp. 409–480, https://doi.org/10.1002/352760264X.ch6. Ch. 6.

[52] P. Hohenberg, W. Kohn, Inhomogeneous electron gas, Phys. Rev. 136 (3B) (1964) B864–B871, https://doi.org/10.1103/PhysRev.136.B864.

[53] W. Kohn, L.J. Sham, Self-consistent equations including exchange and correlation effects, Phys. Rev. 140 (4A) (1965) A1133–A1138, https://doi.org/10.1103/PhysRev.140.A1133.

[54] J.P. Perdew, K. Burke, M. Ernzerhof, Generalized gradient approximation made simple, Phys. Rev. Lett. 77 (18) (1996) 3865–3868, https://doi.org/10.1103/PhysRevLett.77.3865.

[55] G. Kresse, J. Hafner, Ab initio molecular dynamics for open-shell transition metals, Phys. Rev. B 48 (17) (1993) 13115–13118, https://doi.org/10.1103/PhysRevB.48.13115.

[56] G. Kresse, J. Furthmüller, Efficient iterative schemes for ab initio total-energy calculations using a plane-wave basis set, Phys. Rev. B 54 (16) (1996) 11169–11186, https://doi.org/10.1103/PhysRevB.54.11169.

[57] P.E. Blöchl, Projector augmented-wave method, Phys. Rev. B 50 (24) (1994) 17953–17979, https://doi.org/10.1103/physrevb.50.17953.

[58] L.G. Ferreira, M. Marques, L.K. Teles, Slater half-occupation technique revisited: the LDA-1/2 and GGA-1/2 approaches for atomic ionization energies and band gaps in semiconductors, AIP Adv. 1 (3) (2011) 032119, https://doi.org/10.1063/1.3624562.

[59] L.G. Ferreira, R.R. Pelá, L.K. Teles, M. Marques, M. Ribeiro Jr., J. Furthmüller, The LDA-1/2 technique: recent developments, AIP Conf. Proc. 1566 (1) (2013) 27–28, https://doi.org/10.1063/1.4848268.

[60] J.C. Slater, K.H. Johnson, Self-consistent-field X–α cluster method for polyatomic molecules and solids, Phys. Rev. B 5 (3) (1972) 844–853, https://doi.org/10.1103/PhysRevB.5.844.

[61] J.F. Janak, Proof that $\partial E/\partial n_i = \varepsilon_i$ in density-functional theory, Phys. Rev. B 18 (12) (1978) 7165–7168, https://doi.org/10.1103/PhysRevB.18.7165.

[62] L. Yu, A. Zunger, Identification of potential photovoltaic absorbers based on first-principles spectroscopic screening of materials, Phys. Rev. Lett. 108 (6) (2012) 068701, https://doi.org/10.1103/physrevlett.108.068701.

[63] W. Shockley, H.J. Queisser, Detailed balance limit of efficiency of p-n junction solar cells, J. Appl. Phys. 32 (3) (1961) 510–519, https://doi.org/10.1063/1.1736034.

[64] M. Barhoumi, First-principles calculations to investigate electronic band structure, optical and mechanical properties of new CaFCl monolayer, Results Phys. 45 (2023) 106251, https://doi.org/10.1016/j.rinp.2023.106251.

[65] W. Diery, Electronic and Optical Properties of New Pentagonal Janus PtXY (X, Y=S, Se, Te; X ≠ Y) Monolayers: A DFT Study, Physica B Condens. Matter 669 (2023) 415308.10.1016/j.physb.2023.4153082023, 415308 10.1016/j.physb.2023.415308 Electronic and optical properties of new pentagonal janus PtXY (X, YS, Se, Te; X≠ Y) monolayers: a DFT study.

[66] M. Gajdoš, K. Hummer, G. Kresse, J. Furthmüller, F. Bechstedt, Linear optical properties in the projector-augmented wave methodology, Phys. Rev. B 73 (4) (2006) 045112, https://doi.org/10.1103/PhysRevB.73.045112.

[67] B.Y. Hu, Kramers-kronig in two lines, Am. J. Phys. 57 (9) (1989) 821, https://doi.org/10.1119/1.15901.

[68] A.C. Dias, J.F. Silveira, F. Qu, WanTiBEXOS: a wannier based tight binding code for electronic band structure, excitonic and optoelectronic properties of solids, Comput. Phys. Commun. 285 (2023) 108636, https://doi.org/10.1016/j.cpc.2022.108636.

[69] C.K. Møller, Crystal structure and photoconductivity of cæsium plumbohalides, Nature 182 (4647) (1958) 1436, https://doi.org/10.1038/1821436a0.

[70] S. Sharma, N. Weiden, A. Weiss, Phase diagrams of quasibinary systems of the type: ABX_3 -A'BX_3; ABX_3 -AB'X_3, and ABX_3 -ABX'$_3$, Z. Phys. Chem. 175 (1992) 63–80.

[71] K. Yamada, S. Funabiki, H. Horimoto, T. Matsui, T. Okuda, S. Ichiba, Structural phase transitions of the polymorphs of $CsSnI_3$ by means of rietveld analysis of the X-Ray diffraction, Chem. Lett. 20 (5) (1991) 801–804, https://doi.org/10.1246/cl.1991.801.

[72] J. Zheng, C.H.A. Huan, A.T.S. Wee, M.H. Kuok, Electronic properties of $CsSnBr_3$: studies by experiment and theory, Surf. Interface Anal. 28 (1) (1999) 81–83, https://doi.org/10.1002/(SICI)1096-9918(199908)28:1<81::AID-SIA623>3.0.CO;2-D.

[73] A.R. Denton, N.W. Ashcroft, Vegard's law, Phys. Rev. A 43 (6) (1991) 3161–3164, https://doi.org/10.1103/physreva.43.3161.

[74] M.B.-L. Cointe, J. Hébert, C. Baldé, N. Moisan, L. Toupet, P. Guionneau, J.F. Létard, E. Freysz, H. Cailleau, E. Collet, Intermolecular control of thermoswitching and photoswitching phenomena in two spin-crossover polymorphs, Phys. Rev. B 85 (6) (2012) 064114, https://doi.org/10.1103/physrevb.85.064114.

[75] E. Collet, P. Guionneau, Structural analysis of spin-crossover materials: from molecules to materials, C. R. Chim. 21 (12) (2018) 1133–1151, https://doi.org/10.1016/j.crci.2018.02.003.

[76] R.C. Remsing, M.L. Klein, A new perspective on lone pair dynamics in halide perovskites, APL Mater. 8 (5) (2020) 050902, https://doi.org/10.1063/5.0001908.

[77] Y. Fu, S. Jin, X.-Y. Zhu, Stereochemical expression of ns_2 electron pairs in metal halide perovskites, Nat. Rev. Chem. 5 (12) (2021) 838–852, https://doi.org/10.1038/s41570-021-00335-9.

[78] T. Li, S. Luo, X. Wang, L. Zhang, Alternative lone-pair ns_2 -cation-based semiconductors beyond lead halide perovskites for optoelectronic applications, Adv. Mater. 33 (32) (2021) 2008574, https://doi.org/10.1002/adma.202008574.

[79] D.S. Aidhy, C. Wolverton, First-principles prediction of phase stability and crystal structures in Li-Zn and Na-Zn mixed-metal borohydrides, Phys. Rev. B 83 (14) (2011) 144111, https://doi.org/10.1103/physrevb.83.144111.

[80] M. Worsdale, A. Rabis, E. Fabbri, T.J. Schmidt, D. Kramer, Conductivity limits of extrinsically doped SnO_2 supports, ECS Trans. 69 (17) (2015) 1167–1178, https://doi.org/10.1149/06917.1167ecst.

[81] Y. Kim, Effect of metal composition on the structure of layer-structured cathode materials for Li-ion batteries, Appl. Phys. A 126 (7) (2020) 556, https://doi.org/10.1007/s00339-020-03744-7.

[82] C.J. Bartel, Review of computational approaches to predict the thermodynamic stability of inorganic solids, J. Mater. Sci. 57 (23) (2022) 10475–10498, https://doi.org/10.1007/s10853-022-06915-4.

[83] A. Manzoor, S. Pandey, D. Chakraborty, S.R. Phillpot, D.S. Aidhy, Entropy contributions to phase stability in binary random solid solutions, NPJ Comput. Mater Mater 4 (1) (2018) 47, https://doi.org/10.1038/s41524-018-0102-y.

[84] C.C. Stoumpos, C.D. Malliakas, M.G. Kanatzidis, Semiconducting tin and lead iodide perovskites with organic cations: phase transitions, high mobilities, and near-infrared photoluminescent properties, Inorg. Chem. 52 (15) (2013) 9019–9038, https://doi.org/10.1021/ic401215x.

[85] J. Even, L. Pedesseau, J.-M. Jancu, C. Katan, Importance of spin-orbit coupling in hybrid organic/inorganic perovskites for photovoltaic applications, J. Phys. Chem. Lett. 4 (17) (2013) 2999–3005, https://doi.org/10.1021/jz401532q.

[86] S.X. Tao, X. Cao, P.A. Bobbert, Accurate and efficient band gap predictions of metal halide perovskites using the DFT-1/2 method: GW accuracy with DFT expense, Sci. Rep. 7 (1) (2017) 14386, https://doi.org/10.1038/s41598-017-14435-4.

[87] W. Geng, C. Tong, Y. Zhang, L. Liu, Theoretical progress on the relationship between the structures and properties of perovskite solar cells, Adv. Theory Simul. 3 (9) (2020) 2000022, https://doi.org/10.1002/adts.202000022.

[88] P.P. Ingole, G.B. Markad, D. Saraf, L. Tatikondewar, O. Nene, A. Kshirsagar, S. K. Haram, Band GAp Bowing at Nanoscale: Investigation of CsS_x Se_{1-x} alloy quantum dots through cyclic voltammetry and density functional theory, J. Phys. Chem. C. 117 (14) (2013) 7376–7383, https://doi.org/10.1021/jp400021u.

[89] A. Rajagopal, R.J. Stoddard, H.W. Hillhouse, A.K.-Y. Jen, On understanding bandgap bowing and optoelectronic quality in Pb—Sn alloy hybrid perovskites, J. Mater. Chem. A 7 (27) (2019) 16285–16293, https://doi.org/10.1039/c9ta05308e.

[90] S. Khatun, A. Maiti, A.J. Pal, Bowing of transport gap in hybrid halide perovskite alloys (CH_3 NH_3 Sn_{1-x} Pb_x I_3): which band is responsible, Appl. Phys. Lett. 116 (1) (2020) 012104, https://doi.org/10.1063/1.5134749.

[91] J. Im, C.C. Stoumpos, H. Jin, A.J. Freeman, M.G. Kanatzidis, Antagonism between spin-orbit coupling and steric effects causes anomalous band gap evolution in the perovskite photovoltaic materials CH_3 NH_3 Sn_{1-x} Pb_x I_3, J. Phys. Chem. Lett. 6 (17) (2015) 3503–3509, https://doi.org/10.1021/acs.jpclett.5b01738.

[92] N.K. Noel, S.D. Stranks, A. Abate, C. Wehrenfennig, S. Guarnera, A.-A. Haghighirad, A. Sadhanala, G.E. Eperon, S.K. Pathak, M.B. Johnston, A. Petrozza, L.M. Herz, H.J. Snaith, Lead-free organic-inorganic tin halide perovskites for photovoltaic applications, Energy Environ. Sci. 7 (9) (2014) 3061–3068, https://doi.org/10.1039/C4EE01076K.

[93] Y. Zhou, Y. Zhao, Chemical stability and instability of inorganic halide perovskites, Energy Environ. Sci. 12 (5) (2019) 1495–1511, https://doi.org/10.1039/C8EE03559H.

[94] H. Li, Q. Wei, Z. Ning, Toward high efficiency tin perovskite solar cells: a perspective, Appl. Phys. Lett. 117 (6) (2020) 060502, https://doi.org/10.1063/5.0014804.

[95] Y. Ogomi, A. Morita, S. Tsukamoto, T. Saitho, N. Fujikawa, Q. Shen, T. Toyoda, K. Yoshino, S.S. Pandey, T. Ma, S. Hayase, CH_3 NH_3 Sn_x $Pb_{(1-x)}$ I_3 Perovskite solar cells covering up to 1060 nm, J. Phys. Chem. Lett. 5 (6) (2014) 1004–1011, https://doi.org/10.1021/jz5002117.

[96] F. Liu, C. Ding, Y. Zhang, T.S. Ripolles, T. Kamisaka, T. Toyoda, S. Hayase, T. Minemoto, K. Yoshino, S. Dai, M. Yanagida, H. Noguchi, Q. Shen, Colloidal synthesis of air-stable alloyed $CsSn_{1-x}$ Pb_x I_3 perovskite nanocrystals for use in solar cells, J. Am. Chem. Soc. 139 (46) (2017) 16708–16719, https://doi.org/10.1021/jacs.7b08628.

[97] A. Babayigit, A. Ethirajan, M. Muller, B. Conings, Toxicity of organometal halide perovskite solar cells, Nat. Mater. 15 (3) (2016) 247–251, https://doi.org/10.1038/nmat4572.

[98] I.R. Benmessaoud, A.-L. Mahul-Mellier, E. Horváth, B. Maco, M. Spina, H. A. Lashuel, L. Forró, Health hazards of methylammonium lead iodide based perovskites: cytotoxicity studies, Toxicol. Res. 5 (2) (2016) 407–419, https://doi.org/10.1039/c5tx00303b.

[99] H. Hu, B. Dong, W. Zhang, Low-toxic metal halide perovskites: opportunities and future challenges, J. Mater. Chem. A 5 (2017) 11436–11449, https://doi.org/10.1039/C7TA00269F.